2019

Atomic-Scale Structure of Mesoporous Silica-Encapsulated Pt and PtSn Nanoparticles Revealed by Dynamic Nuclear Polarization-Enhanced Si-29 MAS NMR Spectroscopy

Evan Wenbo Zhao
University of Florida

Raghu Maligal-Ganesh
Iowa State University

Frederic Mentink-Vigier
National High Magnetic Field Laboratory

Tommy Yunpu Zhao
University of Florida

Tong Qi
University of Florida

See next page for additional authors

Atomic-Scale Structure of Mesoporous Silica-Encapsulated Pt and PtSn Nanoparticles Revealed by Dynamic Nuclear Polarization-Enhanced Si-29 MAS NMR Spectroscopy

Abstract
Mesoporous silica encapsulated Pt (Pt@mSiO2) and PtSn (PtSn@mSiO2) nanoparticles (NPs) are representatives of a novel class of heterogeneous catalysts with uniform particle size, enhanced catalytic properties, and superior thermal stability. In the ship-in-a-bottle synthesis, PtSn@mSiO2intermetallic NPs are derived from Pt@mSiO2 seeds where the mSiO2 shell is formed by polymerization of tetraethyl orthosilicate around a tetradecyltrimethylammonium bromide template, a surfactant used to template MCM-41. Incorporation of Sn into the Pt@mSiO2 seeds is accommodated by chemical etching of the mSiO2 shell. The effect of this etching on the atomic-scale structure of the mSiO2 has not been previously examined, nor has the extent of the structural similarity to MCM-41. Here, the quaternary Q2, Q3 and Q4 sites corresponding to formulas Si(O1/2)2(OH)2, Si(O1/2)3(OH)1 and Si(O1/2)4, in MCM-41 and the mesoporous silica of Pt@mSiO2 and PtSn@mSiO2 NPs were identified and quantified by conventional and dynamic nuclear polarization enhanced Si-29 Magic Angle Spinning Nuclear Magnetic Resonance (DNP MAS NMR). The connectivity of the -Si-O-Si- network was revealed by DNP enhanced two-dimensional 29Si-29Si correlation spectroscopy.

Keywords
Pt-Sn intermetallic nanoparticles, mesoporous silica, 29Si NMR, solid-state nuclear magnetic resonance, dynamic nuclear polarization

Disciplines
Materials Chemistry

Comments
This document is the unedited Author's version of a Submitted Work that was subsequently accepted for publication in *Journal of Physical Chemistry C*, copyright © 2019 American Chemical Society after peer review. To access the final edited and published work see DOI: 10.1021/acs.jpcc.9b01782.

Authors
Evan Wenbo Zhao, Raghu Maligal-Ganesh, Frederic Mentink-Vigier, Tommy Yunpu Zhao, Yong Du, Yuchen Pei, Wenyu Huang, and Clifford Russell Bowers

Atomic-Scale Structure of Mesoporous Silica-Encapsulated Pt and PtSn Nanoparticles Revealed by Dynamic Nuclear Polarization-Enhanced Si-29 MAS NMR Spectroscopy

Evan Wenbo Zhao,[1,#,] Raghu Maligal-Ganesh,[2] Frederic Mentink-Vigier,[3] Tommy Yunpu Zhao,[1] Yong Du,[1] Yuchen Pei,[2] Wenyu Huang,[2,4,*] Clifford Russell Bowers[1,*]*

[1]Department of Chemistry, University of Florida, Gainesville, Florida, 32611 United States.

[2]Department of Chemistry, Iowa State University, Ames, Iowa, 50011 United States.

[3]National High Magnetic Field Laboratory, Tallahassee, Florida 32310 United States.

[4]Ames Laboratory, U.S. Department of Energy, Ames, Iowa 50011 United States.

[#]Present Address: Department of Chemistry, University of Cambridge, Cambridge, CB2 1EW, United Kingdom.

*Correspondence to: zhao0110@chem.ufl.edu, whuang@iastate.edu, bowers@chem.ufl.edu.

ABSTRACT. Mesoporous silica encapsulated Pt (Pt@$mSiO_2$) and PtSn (PtSn@$mSiO_2$) nanoparticles (NPs) are representatives of a novel class of heterogeneous catalysts with uniform particle size, enhanced catalytic properties, and superior thermal stability. In the ship-in-a-bottle synthesis, PtSn@$mSiO_2$ intermetallic NPs are derived from Pt@$mSiO_2$ seeds where the $mSiO_2$ shell is formed by polymerization of tetraethyl orthosilicate around a tetradecyltrimethylammonium bromide template, a surfactant used to template MCM-41. Incorporation of Sn into the Pt@$mSiO_2$ seeds is accommodated by chemical etching of the $mSiO_2$ shell. The effect of this etching on the atomic-scale structure of the $mSiO_2$ has not been previously examined, nor has the extent of the structural similarity to MCM-41. Here, the quaternary Q^2, Q^3 and Q^4 sites corresponding to formulas $Si(O_{1/2})_2(OH)_2$, $Si(O_{1/2})_3(OH)_1$ and $Si(O_{1/2})_4$, in MCM-41 and the mesoporous silica of Pt@$mSiO_2$ and PtSn@$mSiO_2$ NPs were identified and quantified by conventional and dynamic nuclear polarization enhanced Si-29 Magic Angle Spinning Nuclear Magnetic Resonance (DNP MAS NMR). The connectivity of the -Si-O-Si- network was revealed by DNP enhanced two-dimensional ^{29}Si-^{29}Si correlation spectroscopy.

KEYWORDS: Pt-Sn intermetallic nanoparticles, mesoporous silica, ^{29}Si NMR, solid-state nuclear magnetic resonance, dynamic nuclear polarization.

INTRODUCTION

Encapsulation of transition metal nanoparticles in mesoporous silica ($mSiO_2$) has been found to be beneficial for diverse applications ranging from catalysis[1-3] to colorimetric diagnostics,[4] SERS detection[5] and photothermal therapy.[6] The $mSiO_2$ shell can impart improved thermal stability and tunable optical properties, as well as facilitate functionalization of encapsulated materials.[7] In the "ship-in-a-bottle" approach to the synthesis of nanoparticles with ordered intermetallic phases, $mSiO_2$ encapsulation protects the metallic cores from sintering during the high-temperature treatment, yet the shell does not block access of small organic substrates/products to/from the catalytically active sites.[8]

The intermetallic nanoparticles (iNPs) such as PtSn@$mSiO_2$ exhibit increased selectivity and stability in selective hydrogenations, dehydrogenation, and CO oxidation.[1, 9-10] The PtSn@$mSiO_2$ iNP catalyst was also found to be highly selective in the hydrogenation of nitro groups in various functionalized nitroarenes.[9] Recently, we demonstrated the efficacy of PtSn@$mSiO_2$ and Pt_3Sn@$mSiO_2$ NPs for hyperpolarization by parahydrogen induced polarization (PHIP).[11-13] In particular, the PtSn@$mSiO_2$ iNPs delivered record-high pairwise selectivity in the heterogeneous hydrogenation of propene to propane,[14] and the Pt_3Sn@$mSiO_2$ iNPs were found to be unique in their ability to mediate the conversion of the NMR-invisible parahydrogen singlet spin order into hyperpolarized proton magnetization of co-adsorbed water, methanol, and ethanol.[13]

The $mSiO_2$ shell around our Pt NPs is formed by polymerization of tetraethyl orthosilicate (TEOS) at room temperature in the presence of a base with the cationic surfactant tetradecyltrimethylammonium bromide (TTAB) functioning as the template. The PtSn@$mSiO_2$ iNPs are prepared by heterogeneous nucleation of Sn from its hydrated salt $SnCl_2 \cdot 2H_2O$ at the metal surface of Pt@$mSiO_2$ in tetraethylene glycol at 280 °C. This ship-in-a-bottle synthesis was

first employed to prepare bimetallic PtPd from Pt@mSiO$_2$ seeds[11] where it was observed that the silica shells are thinned and eventually completely etched away when excess Pd precursor (as K_2PdCl_4) was used. The dissolution of silica was further confirmed by inductively coupled plasma mass spectrometry. However, despite its key role in the synthesis, stability and catalytic properties, little is known about the atomic-scale structure within the mSiO$_2$ shell of Pt@mSiO$_2$ or PtSn@mSiO$_2$, and the possible compositional and structural changes that might occur with the chemical etching accompanying incorporation of Sn into Pt@mSiO$_2$ seed particles has not been previously investigated. While the mSiO$_2$ shell is clearly visible in TEM images and the elemental distribution has been mapped out by energy-dispersive X-ray spectroscopy,[15] these techniques do not provide information about the atomic-scale structure, where diffraction techniques (e.g., Powder X-ray diffraction crystallography) are inapplicable. Consequently, the bonding topologies of Si within the mSiO$_2$ encapsulation shells and at the mSiO$_2$/metal interfaces in the Pt@mSiO$_2$ and PtSn@mSiO$_2$ NPs have eluded characterization until now.

NMR spectroscopy can provide atomic-scale structural information in solids which lack long-range order, which make it well-suited for the characterization of surfaces of catalysts and NP-adsorbate interactions. However, in comparison to standard surface science techniques, conventional NMR methods are often inapplicable because of the inherently low sensitivity due to the unfavorable Boltzmann equilibrium polarization of nuclear spins. In Dynamic Nuclear Polarization (DNP), nuclear spin hyperpolarization (i.e. enhanced, non-thermal equilibrium nuclear spin polarization) is induced by continuous microwave saturation of the unpaired electron-spin resonance transition and electron-nuclear cross-relaxation.[16-17] When combined with cross-polarization (CP), DNP Magic Angle Spinning (MAS) NMR spectroscopy typically affords a 1-2 orders of magnitude boost in sensitivity with spatial selectivity to atoms residing at or near the

surface, which provides a powerful contrast enhancement for probing surface structure, surface-adsorbate interactions, and catalytically active sites.[18-31] DNP MAS NMR has been recently applied to functionalized silica and SiO_x/Al_2O_3 materials to obtain chemical bonding information.[18-19, 32-36]

Here we present the results of both conventional and Si-29 DNP MAS NMR experiments on Pt@mSiO$_2$, PtSn@mSiO$_2$, and MCM-41 aimed at comparing the atomic-scale structure of the mesoporous silica in these three materials. Of particular interest are the possible changes in the distribution of Q^x functionalities (where Q signifies a quaternary Si atom bonded to four oxygen atoms and *x* refers to the number of other Q units connected to the Si tetrahedron) induced upon incorporation of Sn into Pt@mSiO$_2$ seed particles. We obtained the distribution of Si functionalities and Q^x network connectivity was revealed by a combination of one and two-dimensional (2D) MAS NMR techniques. Significant differences might exist in the Si bonding distributions due to the geometrical curvature of the metal nanoparticle surfaces and the chemical etching of the inner silica layers accompanying incorporation of Sn into Pt@mSiO$_2$ seed particles. Two different biradical molecules, AMUPol[37] and TEKPol[38] (see Figure S3), were separately introduced into samples of the solid powders by incipient wetness impregnation.[18] We compare the structure and composition of the mesoporous silica shells encapsulating Pt and PtSn NPs to MCM-41 which is included in this study as a reference material that has been extensively studied by MAS NMR.[39-45] The silica in all three materials was templated from the tetraalkylammonium salts TTAB (Pt@mSiO$_2$ and PtSn@mSiO$_2$) and CTAB (MCM-41), following which they were subjected to identical post-synthetic oxidation in air at 500 °C and reduction in H_2/He at 300 °C prior to the NMR experiments.

RESULTS AND DISCUSSION

Morphology and Porosity of the Nanoparticles. In the TEM images of the Pt@mSiO$_2$ and PtSn@mSiO$_2$ NPs presented in Fig. 1A and B, respectively, the silica shells have a granulated and disordered appearance. The Pt@mSiO$_2$ seed NPs have an average metal core of 14.3 $\pm$ 0.8 nm in diameter and a SiO$_2$ shell of roughly 10.9 ± 0.8 nm in thickness. The PtSn@mSiO$_2$ NPs have a larger average metal core of 20.6 $\pm$ 0.9 nm in diameter. The observably thinner SiO$_2$ shell thickness of 8.3 ± 0.8 nm results from chemical etching during the incorporation of Sn into the metal core. As seen in the high-angle annular dark field scanning TEM (HAADF-STEM) and EDS elemental mapping of PtSn@mSiO$_2$ in Fig. 1C-H, the SiO$_2$ shell encapsulates the PtSn metal core. The well-defined channels in MCM-41[46] are not observed in the TEM images of the mSiO$_2$ shells of our Pt@mSiO$_2$ and PtSn@mSiO$_2$ samples. Although MCM-41 has a significantly higher specific surface area due to the presence of the non-porous metal NPs in the catalysts, the mesoporous silicas in all three samples have a similar pore of around 2.4 nm in diameter (Fig. 2 and Table 1). Neither TEM nor EDS elemental mapping provides information about the atomic-scale bonding in the amorphous silica.[14]

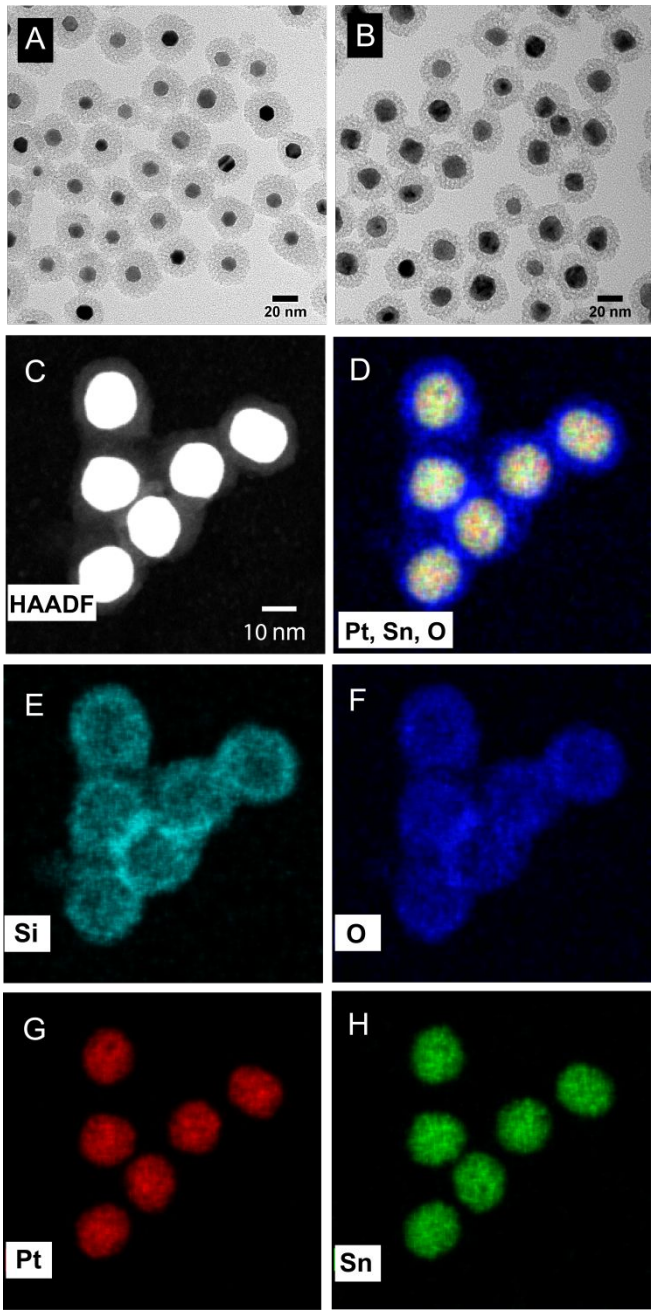

Figure 1. TEM images of (A) Pt@mSiO$_2$ and (B) PtSn@mSiO$_2$ NPs. (C) HAADF-STEM image of the PtSn@mSiO$_2$ iNPs. (D-H) EDS elemental mappings of the PtSn@mSiO$_2$ iNPs.

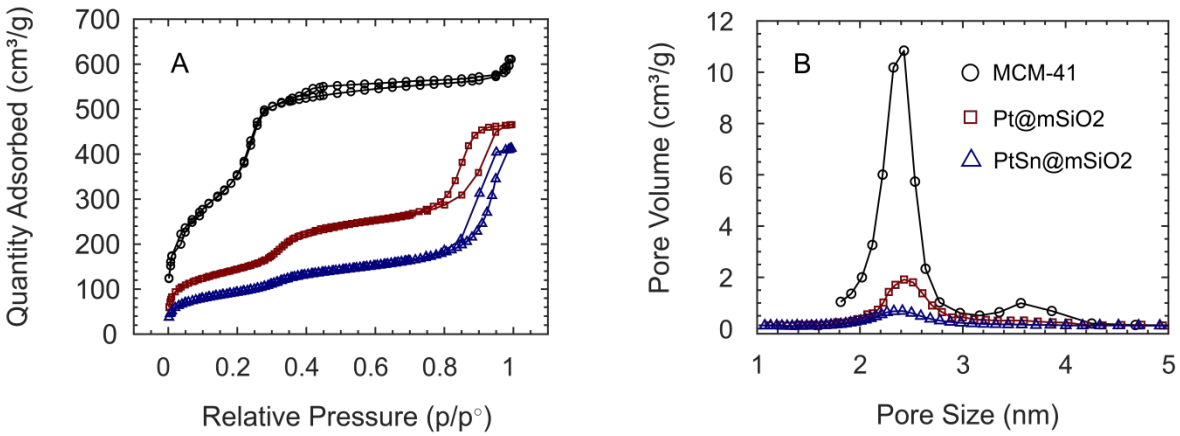

Figure 2. (A) N_2 sorption isotherms at 77 K and (B) BJH pore size distributions of MCM-41, Pt@mSiO$_2$ and PtSn@mSiO$_2$, respectively. The total adsorbed N_2 and pore volume are divided by the total mass of the catalysts.

Table 1. Summary of physisorption measurements.

Sample	**BET Surface Area (m^2/g)**	**Pore Volume (cm^3/g)**	**Pore Size (nm)**
MCM-41	~1160	0.97	2.4
Pt@mSiO$_2$	~506	0.69	2.4
PtSn@mSiO$_2$	~329	0.48	2.4

Conventional ^{29}Si MAS NMR. Prior to the NMR experiments, Pt@mSiO$_2$, PtSn@mSiO$_2$ NPs and MCM-41 were oxidized in air at 500 °C and reduced in H_2/Ar (5/45 mL/min) at 300 °C for four hours, which is a standard pretreatment for the catalysts. The room-temperature 1D ^{29}Si MAS NMR spectra of two different synthetic batches of Pt@mSiO$_2$, PtSn@mSiO$_2$ NPs and MCM-41 were recorded prior to impregnation with radicals and are presented in Fig. 3 and Fig. S1, respectively. The multi-peak fitting of the spectral region corresponding to the Q^x sites yields three peaks: Q^2 at -90 ppm; Q^3 at -100 ppm; and Q^4 at -109 ppm.[28, 47]

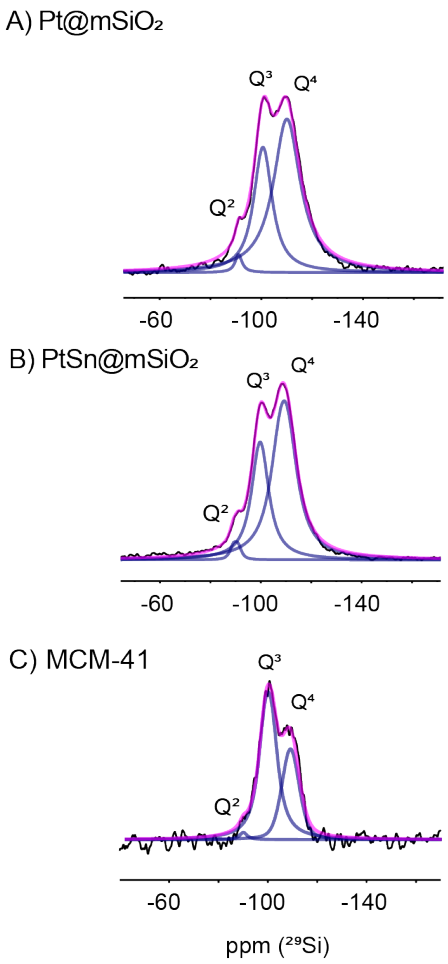

Figure 3. Room temperature 1D single-pulse ^{29}Si MAS NMR spectra of (A) $Pt@mSiO_2$ (batch #1), (B) $PtSn@mSiO_2$ (batch #1) and (C) MCM-41. These spectra were recorded prior to impregnation of radicals. Black: experimental spectra. Magenta: fitted spectra. Blue: spectral components resulting from the multi-peak fitting.

Table 2. Fraction of the Q^x sites calculated from the integration of the individual components of the multi-peak fitting decomposition analysis.

NP Type	Batch Number	% Q^2 (-90 ppm)	% Q^3 (-100 ppm)	% Q^4 (-109 ppm)
Pt@$mSiO_2$	1st	1.5 ± 0.24	36.2 ± 2.2	62.3 ± 2.5
Pt@$mSiO_2$	2nd	1.9 ± 0.7	25.4 ± 2.2	72.7 ± 3.7
PtSn@$mSiO_2$	1st	1.7 ± 0.5	37.0 ± 2.4	61.3 ± 4.1
PtSn@$mSiO_2$	2nd	1.8 ± 0.9	37.5 ± 1.7	60.7 ± 1.6
MCM-41	1st	1.6 ± 0.1	61.7 ± 2.8	36.6 ± 3.8

The peak areas in Table 2 are proportional to the number of Q^x sites of each type. The Q^3 and Q^4 sites comprise approximately 98% of all the silicon atoms in both the Pt and PtSn NPs as well as MCM-41, while Q^2 sites are present at a level of only a few percent. The pore sizes of the mesoporous shells in the Pt@$mSiO_2$ and PtSn@$mSiO_2$ samples, as measured by N_2 physisorption analysis, are 2.4 nm respectively. Despite significantly different $mSiO_2$ shell thicknesses, our results show that the Pt@$mSiO_2$ and PtSn@$mSiO_2$ NPs have a similar distribution of Q^x sites. Our MCM-41 sample also has a pore size of 2.4 nm. The chemical shifts of the Q^x sites in MCM-41 were found to be close to those of ^{29}Si in the silica shells of Pt and PtSn iNPs, validating the compositional similarity. The measured ratios Q^3/Q^4 in site densities in the Pt@$mSiO_2$ and PtSn@$mSiO_2$ are similar, with a greater density of Q^4 over Q^3 sites by almost a factor of two. In contrast, the MCM-41 sample has a greater density of Q^3 over Q^4 sites (see Table 2). This high Q^3/Q^4 ratio difference could be attributed to the different synthesis conditions, since MCM-41 was synthesized at 80 °C instead of room temperature used in the growth of $mSiO_2$ for Pt@$mSiO_2$. Additionally, the different Q^3/Q^4 ratios could also be due to differences in the packing of silica

around the curved nanoparticle surface. The $mSiO_2$ encapsulation shell surrounding the metal nanoparticles must accommodate curvature, which precludes the formation of a regular hexagonal arrangement of cylindrical pores that characterizes the MCM-41 family of silicas. This likely explains why such channel structures are not observed in the TEM images of our Pt@$mSiO_2$ and PtSn@$mSiO_2$ samples.

To ensure that the relative peak intensities were not significantly distorted due to differences in T_1 spin relaxation, spectra of PtSn@$mSiO_2$ NPs were also recorded using recycle delays of 45 s and 15 s (Fig. S2). The Q^x distributions obtained for the two different recycle delays were not significantly different. The presence of oxygen in the samples, which were packed into the MAS rotors in ambient air, is known to shorten the T_1 relaxation times to a few seconds.[48-49]

DNP ^{29}Si MAS NMR. To examine the chemical origin, spatial distribution, and connectivity of the Q^x sites, ^{29}Si MAS-DNP NMR experiments were performed. Samples were impregnated with either AMUPol or TEKPol. The molecular sizes of these biradicals are estimated from simple molecular mechanics energy optimization to be 1.7-2.3 nm and 2.1-2.4 nm, respectively, depending on conformation (Fig. S3). Since the molecular sizes are comparable to the ~2.4 nm openings of the mesopores (Fig. 2 and Table 1), the extent of the infiltration of the biradicals into the $mSiO_2$ shell is difficult to predict based solely on theoretical estimates of the molecular dimensions. The H_2O and TCE solvent molecules are certainly small enough to diffuse into the mesopores.[50] Thus, even if AMUPol or TEKPol molecules would be excluded from mesopores due to steric interactions, polarization enhancement of the ^{29}Si nuclei within the $mSiO_2$ shell can still be mediated by a combination of relayed spin diffusion and ^{1}H-^{29}Si CP.[51] Figure 4 presents the ^{29}Si DNP CP-MAS spectra acquired using AMUPol-impregnated Pt@$mSiO_2$ and PtSn@$mSiO_2$. Signal enhancement factors are $\epsilon_{\mathrm{on/off}} =$ 10 and 16, respectively. A signal-to-noise

ratio (SNR) of 335, calculated from the peak intensity of the Q^3 sites in PtSn@mSiO$_2$, was obtained after signal averaging for four minutes (16 scans). In contrast, the SNR of only 66 obtained in the conventional Boltzmann-polarized MAS NMR experiment required copious signal averaging for 69 hours. TEKPol-impregnated PtSn@mSiO$_2$ yielded a smaller enhancement factor of only 10 (Fig. S4). Note that the sensitivity gain afforded by DNP comes at the expense of a slightly degraded spectral resolution arising from paramagnetic broadening.

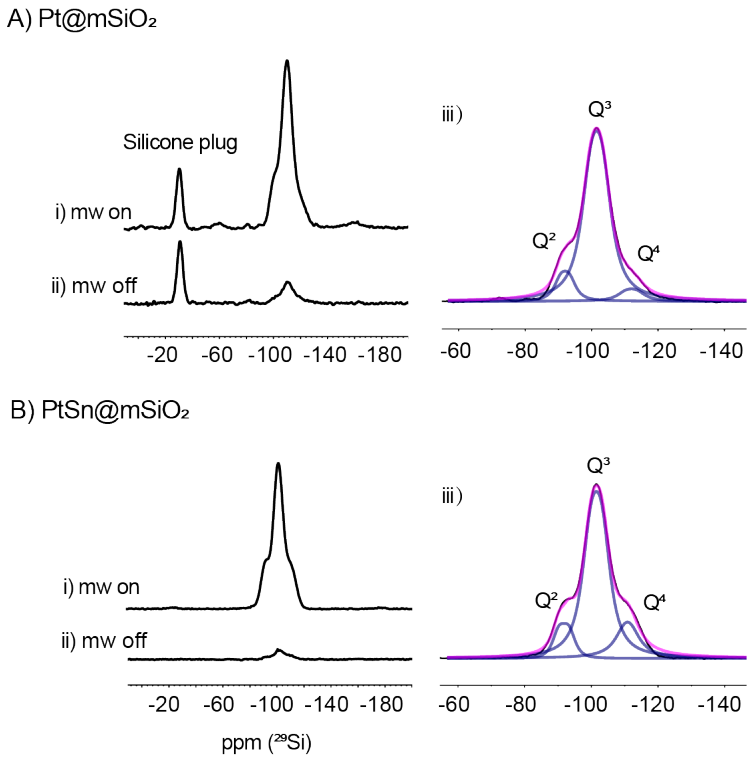

Figure 4. Si-29 DNP CP-MAS spectra of Pt@mSiO$_2$ and PtSn@mSiO$_2$ at 100 K with (i) microwaves on or (ii) microwaves off. (iii) Multi-peak fitting analysis. Black: experimental spectra. Magenta: fitted spectra. Blue: spectral components of the multi-peak fitting.

DNP CP is a two-step process in which the buildup of DNP-enhanced proton polarization is followed by Hartmann-Hahn polarization transfer during a *contact time* (t_c). The CP transfer is mediated by the heteronuclear dipolar coupling and depends on the number of proximal hydrogen atoms and their distances.[52-53] Figure 5 compares the ^{29}Si spectra acquired with direct (via e^--^{29}Si

dipolar couplings) and indirect DNP (via CP with hyperpolarized protons), respectively. The direct DNP spectrum shown in Fig. 5B was collected using a polarization buildup time of 600s. The conventional thermally polarized and direct MAS DNP-NMR spectra are strikingly similar, while the ^{29}Si DNP CP MAS NMR spectrum (Fig. 5C), where only the surface and sub-surface sites within the much shorter range of the ^{1}H-^{29}Si dipolar contact with solvent molecules are expected to be enhanced, is distinctly different. The different line shapes of the direct and indirect DNP spectra indicate an inhomogeneous spatial distribution of the Q^2, Q^3 and Q^4 sites at the pore surface relative to the bulk. The DNP CP experiment yielded relatively strong Q^2 signals, consistent with Q^2 sites located on the pore surface. While the Q^4 sites gave the most intense signals in the direct DNP experiment, these sites yielded relatively weak signals in the indirect DNP experiment, consistent with the high fraction of Q^4 sites which are located away from the pore surface. This further confirms that the Q^4 sites populate the sub-surface regions. Due to the relatively large fraction of Q^3 sites at the pore surface, these sites produced strong signals in both the direct and indirect CP experiments. The spatial distribution of Q^x sites agrees with the established structural model of mesoporous silica.[40, 54]

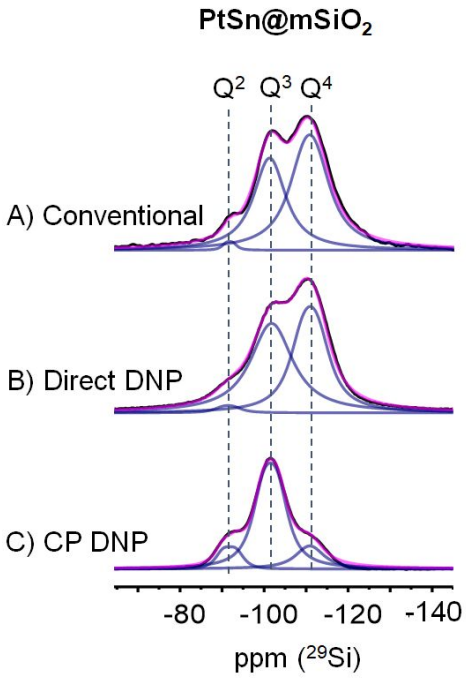

Figure 5. ^{29}Si MAS NMR spectra of PtSn@mSiO$_2$ NPs obtained by (A) a single-pulse without radicals at room temperature (B) direct DNP polarization (C) indirect DNP CP polarization.

^{29}Si-^{29}Si Correlations via CP MAS-DNP NMR. The gain in ^{29}Si NMR sensitivity afforded by DNP CP allowed us to probe the connectivity among the Q^x sites in the PtSn@mSiO$_2$ catalyst using a 2D SR26$_4^{11}$ ^{29}Si-^{29}Si homonuclear correlation experiment. This would have been impractical by conventional MAS NMR with natural abundance ^{29}Si (4.9%) for our samples. The dipolar coupling strength between two ^{29}Si nuclei bonded through an oxygen atom is ≈ -160 Hz (internuclear distance of ~3 Å), which yields a ~1% polarization transfer efficiency when a recoupling time of 2.6 ms is employed in the pulse sequence.[55-56] The internuclear distance between nearest unbonded ^{29}Si nuclei is ~5 Å, and thus the coherence transfer between unbonded Si sites can be safely neglected. The transfer efficiency is further reduced by transverse spin relaxation. The T_2' dephasing time in the PtSn@mSiO$_2$ NPs was measured to be 4 ms in a spin-echo experiment, which is significantly shortened by the impregnated radicals. Therefore, the 2D correlation experiments selectively probe only the ^{29}Si spin pairs bonded via one oxygen atom. In

Fig. 6A, the isotropic chemical shift of ^{29}Si is shown on the horizontal axis (single quantum coherence) and the sum of the isotropic chemical shifts is shown on the vertical axis (double quantum coherence).

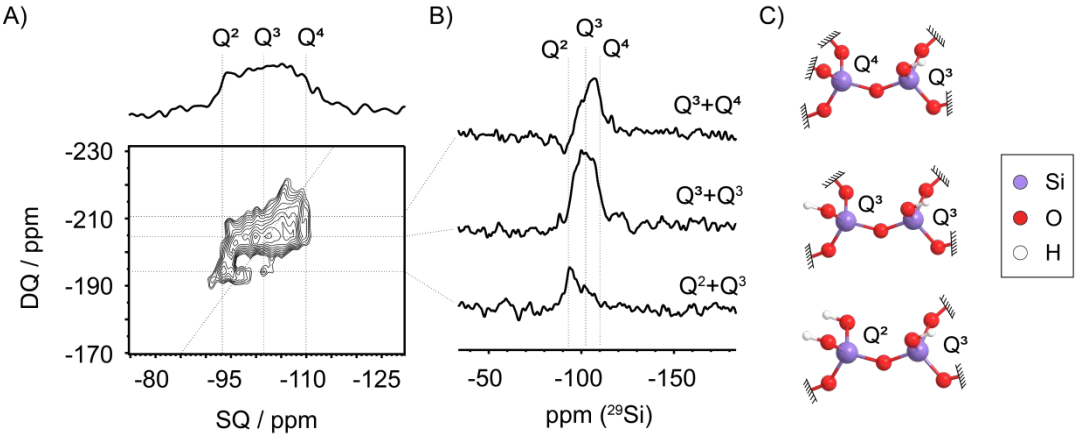

Figure 6. (A) DNP CP enhanced 2D double quantum (DQ) - single quantum (SQ) correlation spectrum collected using the $SR26_4^{11}$ pulse sequence. The sum of the 1D projection along the SQ dimension is shown at the top panel. (B) 1D projection along the SQ dimension at -193 ppm, -204 ppm and -213 ppm in the DQ dimension. (C) Molecular models show the connectivity of the Q sites.

The signals in the spectrum reflect only the bonded ^{29}Si spin pairs. The spectral slices at -193 ppm (Q^2+Q^3), -204 ppm (Q^3+Q^3) and -211 ppm (Q^3+Q^4) are shown in Fig. 6B. The spectra demonstrate Q^2 - Q^3, Q^3 - Q^3 and Q^3 - Q^4 bonding linkages (Fig. 6C). The connectivity agrees with the spatial distribution of the Q^x sites, where Q^2 and Q^3 sites are located at or near the pore surface while Q^4 sites are in the sub-surface region.

CONCLUSIONS

By combining conventional solid-state NMR spectroscopy with direct, indirect, and 2D correlation DNP MAS NMR techniques, differences in surface selectivity were exploited to characterize the atomic-scale chemical structure in the mesoporous silica of the Pt@mSiO_2 and Pt@mSiO_2 catalysts as well as MCM-41. Specifically, the Si Q^2, Q^3 and Q^4 tetrahedra were

identified in the ^{29}Si spectra of the three materials, and the spatial distributions of Q^x sites were deduced. With about 40% of Si sites being Q^2 or Q^3, almost half of silica atoms reside on the surface, implying that an extended network of Q^4 sites does not exist. The results suggest that the overall structure of the SiO_2 shells is very similar to that of typical MCM-41-type materials, except that there is no well-defined periodic pattern of channels. The particular MCM-41 reference sample studied here contained a higher density of Q^3 relative to Q^4 tetrahedra than the $mSiO_2$ shells surrounding the Pt and PtSn nanoparticles which exhibited similar percentages of Q^2, Q^3 and Q^4 Si tetrahedra with Q^4 sites dominating.

Despite significant thinning due to chemical etching of the $mSiO_2$ shell during the incorporation of Sn into the Pt@$mSiO_2$ seed particles, the chemical composition and atomic-scale structure of the $mSiO_2$ shell of Pt@$mSiO_2$ and PtSn@$mSiO_2$ are essentially the same. We conclude that the integrity of the atomic-scale structure of the $mSiO_2$ is preserved through the synthesis of the intermetallic phase. Hence, the different catalytic activities and selectivities of Pt@$mSiO_2$ and PtSn@$mSiO_2$ NPs in various reactions cannot be attributed to structural differences in the $mSiO_2$ shells and must instead be entirely due to the altered chemical composition of the intermetallic phase of the nanoparticle metal core.[14-15, 57] Differences in the spatial selectivity of direct and indirect polarization mechanisms were exploited to probe the spatial distribution of the Q^x sites. The direct DNP and conventional MAS spectra are very similar to each other, whereas the indirect (CP-MAS) DNP spectra are different. The extent to which the radicals penetrate the pores in our materials remains an open question. Most likely, the direct DNP spectra report on the distributions of functionalities across the entire shell, which is similar to mesoporous silica. The Q^4 sites were determined to be buried sub-surface layers while Q^3 and Q^2 sites are present at or near the pore surface. A 2D ^{29}Si-^{29}Si correlation spectrum, enabled by the DNP signal enhancement, revealed

the bonding network connectivity among the Q^x sites in the mesoporous silica shell. The protocols we have presented for the elucidation of the bonding structure should generally be applicable to other silica-encapsulated catalysts as well as other nanomaterials with different metals or core-shell compositions.

EXPERIMENTAL SECTION

Synthesis of Monometallic Pt@mSiO$_2$ NPs. The mSiO$_2$-encapsulated Pt NPs (Pt@mSiO$_2$) were prepared according to a literature protocol.[14] Briefly, around 25 mL of a 10 mM K_2PtCl_4 was added to 200 mL of a 125 mM aqueous solution of tetradecyltrimethylammonium bromide (TTAB). The above mixture was stirred for 10 minutes and then moved to an oil bath maintained at 50 °C for 10 more minutes. 25 mL of 300 mM sodium borohydride solution prepared in ice-cold water (Alfa Aesar, 98%) was then added. After the solution was stirred for 20 h at 50 °C, the dark brown solution was centrifuged at 3000 rpm four times for 30 min, with the supernatant being collected while the residue was discarded. Finally, the supernatant was centrifuged at 14000 rpm for 15 min twice, collected, and re-dispersed in deionized water to obtain around 200 mL of the solution. About 1 mL of a 1 M sodium hydroxide solution was added to obtain a pH between 11 and 12. While stirring, 3 mL of a 10% tetraethyl orthosilicate solution in methanol was added dropwise via syringe. After 24 h, the sample was centrifuged at 14000 rpm twice, and the coated particles (Pt@mSiO$_2$) were redispersed in 200 mL of methanol. To this 10 mL of hydrochloric acid (36% assay) was added and the solution was refluxed at 90 °C for 24 h.

Synthesis of Bimetallic PtSn@mSiO$_2$ NPs. The methanol-dispersed solution of Pt@mSiO$_2$ was centrifuged and redispersed in 75 mL of tetraethylene glycol in a 250 mL two-neck flask. The amount of Pt in a typical synthesis of Pt@mSiO$_2$ particles was 0.15 mmol. PtSn@mSiO$_2$ was made ensuring a Pt:Sn molar ratio of 1:1, using $SnCl_2 \cdot 2H_2O$ (Alfa Aesar, 98%) as the source of Sn, and

heating the solution at 280 °C for 2 hours to form the alloy. The resulting solution was diluted with an equal volume of acetone and centrifuged at 14000 rpm to obtain PtSn@$mSiO_2$ nanoparticles. This was then dried and calcined at 500 °C to remove any organic residues from the synthesis. The sample was then reduced in 10% H_2 in a tube furnace at 300 °C for 4 hours to obtain intermetallic PtSn@$mSiO_2$. Inductively coupled plasma mass spectrometry (ICP-MS) measurements were also carried out on the powdered samples to confirm their stoichiometry as per the synthesis.

Synthesis of MCM-41. Following literature procedures,[46] around 1.0 g of hexadecyltrimethylammonium bromide (CTAB, 2.74 mmol) was dissolved in deionized water (480 mL, 18 MΩ·cm) in a round bottom flask followed by the addition of 3.5 mL of a 2 M solution of NaOH (7.0 mmol). Following stirring of the solution for 1 h at 80 °C, 5.0 mL of tetraethylorthosilicate (TEOS, 22.6 mmol) was then added dropwise over 5 min to the solution. Stirring was continued for an additional 2 h at 80 °C. The solution was filtered, washed with abundant water and methanol, and vacuum dried overnight. The CTAB template was removed by refluxing 1.0 g of dry solid with methanol solution (100 mL) of concentrated HCl (0.8 mL, 9.7 mmol) for 6 h. The surfactant-free sample was then filtered, washed with abundant methanol and water and vacuum dried overnight. The sample was then placed in scintillation vials which were placed in a tube furnace, and pure Ar was passed through the sample at a rate of 50 mL/min for an hour. Following this, the sample was calcined in flowing air at 500 °C for 4 hours to remove any additional CTAB and then reduced at 300 °C for 4 hours in 10% H_2, like the treatments accorded to the Pt@$mSiO_2$ and PtSn@$mSiO_2$ samples ahead of NMR measurements.

Transmission Electron Microscopy (TEM) and Energy-dispersive X-ray Spectroscopy (EDS). TEM images were acquired using a TECNAI G2 F20 at an acceleration voltage of 200 kV,

as reported in earlier work.[14] Prior to TEM measurements, all the samples were first calcined at 500 ˚C and then reduced at the appropriate temperature in a 50 mL/min 10% H_2 in Argon stream. High-resolution transmission electron microscopy (HRTEM), high-angle annular dark field scanning TEM (HAADF-STEM), and elemental mapping analysis were investigated using the same electron microscope equipped with an EDS detector (Oxford INCA EDS) and a Titan Themis 300 probe corrected TEM with a Super-X EDS detector.

Surface Area and Pore Size Measurements. Surface area measurements of Pt@mSiO_2, PtSn@mSiO_2 and MCM-41 were performed by nitrogen sorption isotherms using a Micromeritics 3Flex surface characterization analyzer at 77 K. Prior to surface area measurements, all samples were calcined at 500 °C in air and reduced at 300 °C under 50 mL/min 10% H_2/He in a tube furnace.

Conventional MAS NMR Experiments. Prior to all NMR experiments, Pt@mSiO_2, PtSn@mSiO_2 NPs, and MCM-41 were oxidized in air at 500 ^oC and reduced in H_2 at 300 ^oC for four hours respectively, which is a standard pretreatment of the catalysts. All the conventional 1D ^{29}Si MAS NMR experiment were performed on a Bruker 600 MHz Avance III spectrometer equipped with a 4mm H/F-X solid probe at room temperature with a MAS spinning rate of 8000 Hz. A 90^o pulse with a duration of 4 μs and a recycle delay of 45 s were applied with 3200 scans for Pt@mSiO_2 and 5520 scans for PtSn@mSiO_2. A 30^o pulse with a duration of 2.5 μs and a recycle delay of 30s were applied with 2904 scans for MCM-41. The ^{29}Si chemical shift was calibrated using 3-(trimethylsilyl) propionic-2,2,3,3-d_4 acid sodium salt as a standard, with a ^{29}Si chemical shift at 1.5 ppm.[58] The decompositions of the 1D conventional NMR spectra were carried out in MestReNova 8.0 using the automated algorithm after cubic spline baseline correction. Without changing the chemical shift, the peak height, line width, and Lorentzian/ Gaussian ratio

were varied to optimize the fit for five times Errors of the peak fittings within 90% confidence interval was included into the reported values.

MAS-DNP NMR Experiments. A 30 mg mass of Pt@$mSiO_2$ NPs was impregnated with 30 μL of 10 mM AMUPol solution in a mixture of dimethyl sulfoxide-d_6, H_2O and D_2O at a weight ratio of 8/1/1 in a 1.5 mL centrifuge tube. The damp solid was packed into a 3.2 mm sapphire rotor and sealed with a silicone plug. A 50 mg mass of PtSn@$mSiO_2$ was impregnated with 50 μL of 10 mM AMUPol solution in a mixture of glycerol-d_8, H_2O and D_2O at a weight ratio of 6/1/3. Another 50 mg PtSn@$mSiO_2$ sample was impregnated with 60 μL of 16 mM TEKPol in trichloroethylene (TCE). The two samples were separately packed into 3.2 mm thin-wall zirconia rotors.

All ^{29}Si MAS-DNP experiments were performed on a Bruker 600 MHz/ 395 GHz DNP Avance spectrometer equipped with a 3.2 mm LTMAS probe. For the experiments using AMUPol, 1D ^{29}Si CP MAS experiment on Pt@$mSiO_2$ was performed with the sample spinning at 6000 Hz, a temperature of 100 K and continuous irradiation by microwaves using a gyrotron output power of 6.4 W. The 90° ^{1}H excitation pulse length was 5 μs. A ramped pulse was applied on the ^{1}H channel with a contact time of 4.7 ms. SPINAL64 (83 kHz) was applied for proton decoupling. A recycle delay of 9.1 s was used. The 1D ^{29}Si CP MAS experiments on PtSn@$mSiO_2$ were performed at a spinning speed of 9000 Hz, a 90° ^{1}H excitation pulse length was 3.5 μs, a contact time of 3.6 ms and a recycle delay of 13 s. For the experiments with TEKPol, the 1D ^{29}Si CP MAS spectrum of the impregnated PtSn@$mSiO_2$ sample was performed using the same parameters as in the experiments with AMUPol except for a shorter recycle delay of 2.6 s. The 1D ^{29}Si direct polarization MAS experiment on PtSn@$mSiO_2$ was performed at a spinning rate of 9000 Hz, a temperature of 100 K and continuous microwave irradiation using a gyrotron output power of 6.4 W. A 5 μs 90° pulse tuned at the frequency of ^{29}Si was applied with different recycle delays, as

specified in the results. DNP enhancement factors were calculated by taking the ratio of the peak integrals of the Q sites with microwave on and off. Multi-peak spectral fitting of the 1D Si-29 MAS-DNP NMR spectrum was performed in MestReNova 8.0 by fixing the chemical shift to the value obtained in the conventional spectrum. The peak height, line width and Lorentzian/Gaussian ratio were varied to optimize the fit.

Two-dimensional (2D) ^{29}Si $SR26_4^{11}$ double-quantum (DQ) correlation experiments were performed on PtSn@mSiO_2 (impregnated with AMUPol) at 100 K at a MAS speed of 4000 Hz with continuous microwave irradiation at 6.4 W of gyrotron output power.[55, 59] A 3 μs 90° ^{1}H excitation pulse was applied followed by a ramped CP pulse on the ^{1}H channel with a contact time of 3.7 ms. For the $SR26_4^{11}$ sequence, the duration of 90° ^{29}Si excitation and recoupling pulse was 5 μs and 9.61 ms (nutation frequency is 6.5 times the rotor frequency), respectively. The explicit form of $SR26_4^{11}$ for recoupling and reconversion, respectively, are

$[90_{76.2}270_{256.2}90_{283.9}270_{103.9}]^{13}[90_{283.9}270_{103.9}90_{76.2}270_{256.2}]^{13}$

$[90_{103.9}270_{283.9}90_{256.2}270_{76.2}]^{13}[90_{256.2}270_{76.2}90_{103.9}270_{283.9}]^{13}$

and

$[90_{166.2}270_{346.2}90_{13.9}270_{193.9}]^{13}[90_{13.9}270_{193.9}90_{166.2}270_{346.2}]^{13}$

$[90_{193.9}270_{13.9}90_{346.2}270_{166.2}]^{13}[90_{346.2}270_{166.2}90_{193.9}270_{13.9}]^{13}$

A total of 32 t_1 increments of 225 μs with 1024 scans each were recorded using a recycle delay of 3.64 s. Two sets of spectra acquired under identical conditions were summed to improve the signal-to-noise (SNR) ratio. Pure absorption phase 2D spectra were obtained by the TPPI method in which all pulses prior to the t_1 evolution are given phase shifts in increments of 45° as t_1 is incremented. A cosine Fourier transform was applied in the indirect dimension. cwLg13 and

SPINAL64 (83 kHz) were used for proton decoupling during ^{29}Si dipolar recoupling and data acquisition, respectively.

SUPPORTING INFORMATION

Supporting Information Available: additional conventional and DNP NMR spectra; molecular structures and molecular mechanics energy minimized Van Der Waals surface models of AMUPol and TEKPol.

This material is available free of charge via the Internet at http://pubs.acs.org

ACKNOWLEDGEMENTS

This work was supported by NSF grants CHE-1507230 (CRB) and CHE-1607305 (WH). TYZ acknowledges support from a Center for Condensed Matter Sciences (CCMS) summer fellowship. FMV thanks Daniel Lee for his suggestions setting up SR26. The National High Magnetic Field Laboratory is supported by the NSF (DMR-1157490) and by the State of Florida. The DNP system is funded in part by NIH S10 OD018519 (magnet and console), and NSF CHE-1229170 (gyrotron).

REFERENCES

1. Joo, S. H.; Park, J. Y.; Tsung, C.-K.; Yamada, Y.; Yang, P.; Somorjai, G. A., Thermally Stable Pt/Mesoporous Silica Core–Shell Nanocatalysts For High-Temperature Reactions. *Nature Materials* **2009,** *8* (2), 126-131.
2. Shang, L.; Bian, T.; Zhang, B.; Zhang, D.; Wu, L.-Z.; Tung, C.-H.; Yin, Y.; Zhang, T., Graphene-Supported Ultrafine Metal Nanoparticles Encapsulated by Mesoporous Silica: Robust Catalysts for Oxidation and Reduction Reactions. *Angew. Chem.* **2014,** *126* (1), 254-258.
3. Li, Z.; Mo, L.; Kathiraser, Y.; Kawi, S., Yolk–Satellite–Shell Structured Ni–Yolk@Ni@SiO_2 Nanocomposite: Superb Catalyst toward Methane CO_2 Reforming Reaction. *ACS Catalysis* **2014,** *4* (5), 1526-1536.
4. Liu, S. H.; Han, M. Y., Synthesis, Functionalization, and Bioconjugation of Monodisperse, Silica-Coated Gold Nanoparticles: Robust Bioprobes. *Adv. Funct. Mater.* **2005,** *15* (6), 961-967.
5. Sanles-Sobrido, M.; Exner, W.; Rodríguez-Lorenzo, L.; Rodríguez-González, B.; Correa-Duarte, M. A.; Álvarez-Puebla, R. A.; Liz-Marzán, L. M., Design of SERS-Encoded, Submicron, Hollow Particles Through Confined Growth of Encapsulated Metal Nanoparticles. *J. Am. Chem. Soc.* **2009,** *131* (7), 2699-2705.
6. Radloff, C.; Halas, N., Enhanced Thermal Stability of Silica-Encapsulated Metal Nanoshells. *Appl. Phys. Lett.* **2001,** *79* (5), 674-676.
7. Liu, S.; Han, M. Y., Silica‐Coated Metal Nanoparticles. *Chemistry ‐An Asian Journal* **2010,** *5* (1), 36-45.
8. Dong, B.; Pei, Y.; Zhao, F.; Goh, T. W.; Qi, Z.; Xiao, C.; Chen, K.; Huang, W.; Fang, N., In Situ Quantitative Single-Molecule Study of Dynamic Catalytic Processes in Nanoconfinement. *Nature Catalysis* **2018,** *1*, 135-140.
9. Lu, P.; Campbell, C. T.; Xia, Y., A Sinter-Resistant Catalytic System Fabricated by Maneuvering the Selectivity of SiO_2 Deposition onto the TiO_2 Surface versus the Pt Nanoparticle Surface. *Nano Lett.* **2013,** *13* (10), 4957-4962.
10. Krier, J. M.; Michalak, W. D.; Cai, X.; Carl, L.; Komvopoulos, K.; Somorjai, G. A., Sum Frequency Generation Vibrational Spectroscopy of 1,3-Butadiene Hydrogenation on 4 nm Pt@SiO_2, Pd@SiO_2, and Rh@SiO_2 Core–Shell Catalysts. *Nano Lett.* **2015,** *15* (1), 39-44.
11. Bowers, C. R.; Weitekamp, D. P., Para-Hydrogen and Synthesis Allow Dramatically Enhanced Nuclear Alignment. *Journal of the American Chemical Society* **1987,** *109* (18), 5541-5542.
12. Bowers, C. R.; Weitekamp, D. P., Transformation of Symmetrization Order to Nuclear-Spin Magnetization by Chemical-Reaction and Nuclear-Magnetic-Resonance. *Phys Rev Lett* **1986,** *57* (21), 2645-2648.
13. Zhao, E. W.; Maligal-Ganesh, R.; Du, Y.; Zhao, T. Y.; Collins, J.; Ma, T.; Zhou, L.; Goh, T.-W.; Huang, W.; Bowers, C. R., Surface-Mediated Hyperpolarization of Liquid Water from Parahydrogen. *Chem* **2018,** *4* (6), 1387-1403.
14. Zhao, E. W.; Maligal-Ganesh, R.; Xiao, C.; Goh, T.-W.; Qi, Z.; Pei, Y.; Hagelin-Weaver, H. E.; Huang, W.; Bowers, C. R., Silica-Encapsulated Pt-Sn Intermetallic Nanoparticles: A Robust Catalytic Platform for Parahydrogen-Induced Polarization of Gases and Liquids. *Angewandte Chemie International Edition* **2017,** *56* (14), 3925-3929.

15. Pei, Y.; Qi, Z.; Goh, T. W.; Wang, L.-L.; Maligal-Ganesh, R. V.; MacMurdo, H. L.; Zhang, S.; Xiao, C.; Li, X.; Tao, F.; Johnson, D. D.; Huang, W., Intermetallic Structures with Atomic Precision for Selective Hydrogenation of Nitroarenes. *J. Catal.* **2017,** *356* (Supplement C), 307-314.
16. Overhauser, A. W., Polarization of Nuclei in Metals. *Physical Review* **1953,** *91* (2), 476-476.
17. Carver, T. R.; Slichter, C. P., Polarization of Nuclear Spins in Metals. *Physical Review* **1953,** *92* (1), 212-213.
18. Lelli, M.; Gajan, D.; Lesage, A.; Caporini, M. A.; Vitzthum, V.; Miéville, P.; Héroguel, F.; Rascón, F.; Roussey, A.; Thieuleux, C.; Boualleg, M.; Veyre, L.; Bodenhausen, G.; Coperet, C.; Emsley, L., Fast Characterization of Functionalized Silica Materials by Silicon-29 Surface-Enhanced NMR Spectroscopy Using Dynamic Nuclear Polarization. *Journal of the American Chemical Society* **2011,** *133* (7), 2104-2107.
19. Lee, D.; Monin, G.; Duong, N. T.; Lopez, I. Z.; Bardet, M.; Mareau, V.; Gonon, L.; De Paëpe, G. l., Untangling the Condensation Network of Organosiloxanes on Nanoparticles Using 2D ^{29}Si–^{29}Si Solid-State NMR Enhanced by Dynamic Nuclear Polarization. *Journal of the American Chemical Society* **2014,** *136* (39), 13781-13788.
20. Johnson, R. L.; Perras, F. A.; Kobayashi, T.; Schwartz, T. J.; Dumesic, J. A.; Shanks, B. H.; Pruski, M., Identifying Low-Coverage Surface Species on Supported Noble Metal Nanoparticle Catalysts by DNP-NMR. *Chemical Communications* **2016,** *52* (9), 1859-1862.
21. Perras, F. A.; Padmos, J. D.; Johnson, R. L.; Wang, L.-L.; Schwartz, T. J.; Kobayashi, T.; Horton, J. H.; Dumesic, J. A.; Shanks, B. H.; Johnson, D. D.; Pruski, M., Characterizing Substrate–Surface Interactions on Alumina-Supported Metal Catalysts by Dynamic Nuclear Polarization-Enhanced Double-Resonance NMR Spectroscopy. *J. Am. Chem. Soc.* **2017,** *139* (7), 2702-2709.
22. Ong, T.-C.; Liao, W.-C.; Mougel, V.; Gajan, D.; Lesage, A.; Emsley, L.; Copéret, C., Atomistic Description of Reaction Intermediates for Supported Metathesis Catalysts Enabled by DNP SENS. *Angew. Chem. Int. Ed.* **2016,** *55* (15), 4743-4747.
23. Jin, Y.; Kneusels, N.-J. H.; Marbella, L. E.; Castillo-Martínez, E.; Magusin, P. C. M. M.; Weatherup, R. S.; Jónsson, E.; Liu, T.; Paul, S.; Grey, C. P., Understanding Fluoroethylene Carbonate and Vinylene Carbonate Based Electrolytes for Si Anodes in Lithium Ion Batteries with NMR Spectroscopy. *J. Am. Chem. Soc.* **2018,** *140* (31), 9854-9867.
24. Rossini, A. J., Materials Characterization by Dynamic Nuclear Polarization-Enhanced Solid-State NMR Spectroscopy. *The Journal of Physical Chemistry Letters* **2018,** *9* (17), 5150-5159.
25. Rossini, A. J.; Zagdoun, A.; Lelli, M.; Lesage, A.; Coperet, C.; Emsley, L., Dynamic Nuclear Polarization Surface Enhanced NMR Spectroscopy. *Acc. Chem. Res.* **2013,** *46* (9), 1942-1951.
26. Maly, T.; Debelouchina, G. T.; Bajaj, V. S.; Hu, K.-N.; Joo, C.-G.; Mak–Jurkauskas, M. L.; Sirigiri, J. R.; Wel, P. C. A. v. d.; Herzfeld, J.; Temkin, R. J.; Griffin, R. G., Dynamic Nuclear Polarization at High Magnetic Fields. *The Journal of Chemical Physics* **2008,** *128* (5), 052211.
27. Kobayashi, T.; Perras, F. A.; Slowing, I. I.; Sadow, A. D.; Pruski, M., Dynamic Nuclear Polarization Solid-State NMR in Heterogeneous Catalysis Research. *ACS Catalysis* **2015,** *5* (12), 7055-7062.
28. Al Othman, Z.; Apblett, A. W., Synthesis of Mesoporous Silica Grafted with 3-Glycidoxypropyltrimethoxy–Silane. *Mater. Lett.* **2009,** *63* (27), 2331-2334.

29. Lange, S.; Linden, A. H.; Akbey, Ü.; Trent Franks, W.; Loening, N. M.; Rossum, B.-J. v.; Oschkinat, H., The Effect of Biradical Concentration on The Performance of DNP-MAS-NMR. *Journal of Magnetic Resonance* **2012,** *216* (Supplement C), 209-212.
30. Takahashi, H.; Fernández-de-Alba, C.; Lee, D.; Maurel, V.; Gambarelli, S.; Bardet, M.; Hediger, S.; Barra, A.-L.; De Paëpe, G., Optimization of An Absolute Sensitivity In a Glassy Matrix During DNP-Enhanced Multidimensional Solid-State NMR Experiments. *Journal of Magnetic Resonance* **2014,** *239* (Supplement C), 91-99.
31. Kobayashi, T.; Lafon, O.; Lilly Thankamony, A. S.; Slowing, I. I.; Kandel, K.; Carnevale, D.; Vitzthum, V.; Vezin, H.; Amoureux, J.-P.; Bodenhausen, G.; Pruski, M., Analysis of Sensitivity Enhancement by Dynamic Nuclear Polarization in Solid-State NMR: A Case Study of Functionalized Mesoporous Materials. *PCCP* **2013,** *15* (15), 5553-5562.
32. Mouat, A. R.; George, C.; Kobayashi, T.; Pruski, M.; Van Duyne, R. P.; Marks, T. J.; Stair, P. C., Highly Dispersed SiO_x/Al_2O_3 Catalysts Illuminate The Reactivity of Isolated Silanol Sites. *Angew. Chem.* **2015,** *127* (45), 13544-13549.
33. Gajan, D.; Schwarzwälder, M.; Conley, M. P.; Grüning, W. R.; Rossini, A. J.; Zagdoun, A.; Lelli, M.; Yulikov, M.; Jeschke, G.; Sauvée, C.; Ouari, O.; Tordo, P.; Veyre, L.; Lesage, A.; Thieuleux, C.; Emsley, L.; Copéret, C., Solid-Phase Polarization Matrixes for Dynamic Nuclear Polarization from Homogeneously Distributed Radicals in Mesostructured Hybrid Silica Materials. *J. Am. Chem. Soc.* **2013,** *135* (41), 15459-15466.
34. Berruyer, P.; Lelli, M.; Conley, M. P.; Silverio, D. L.; Widdifield, C. M.; Siddiqi, G.; Gajan, D.; Lesage, A.; Copéret, C.; Emsley, L., Three-Dimensional Structure Determination of Surface Sites. *J. Am. Chem. Soc.* **2017,** *139* (2), 849-855.
35. Kobayashi, T.; Perras, F. A.; Goh, T. W.; Metz, T. L.; Huang, W.; Pruski, M., DNP-Enhanced Ultrawideline Solid-State NMR Spectroscopy: Studies of Platinum in Metal–Organic Frameworks. *The Journal of Physical Chemistry Letters* **2016,** *7* (13), 2322-2327.
36. Kumar, A.; Walder, B. J.; Kunhi Mohamed, A.; Hofstetter, A.; Srinivasan, B.; Rossini, A. J.; Scrivener, K.; Emsley, L.; Bowen, P., The Atomic-Level Structure of Cementitious Calcium Silicate Hydrate. *The Journal of Physical Chemistry C* **2017,** *121* (32), 17188-17196.
37. Sauvée, C.; Rosay, M.; Casano, G.; Aussenac, F.; Weber, R. T.; Ouari, O.; Tordo, P., Highly Efficient, Water-Soluble Polarizing Agents for Dynamic Nuclear Polarization at High Frequency. *Angewandte Chemie International Edition* **2013,** *52* (41), 10858-10861.
38. Zagdoun, A.; Casano, G.; Ouari, O.; Schwarzwälder, M.; Rossini, A. J.; Aussenac, F.; Yulikov, M.; Jeschke, G.; Copéret, C.; Lesage, A.; Tordo, P.; Emsley, L., Large Molecular Weight Nitroxide Biradicals Providing Efficient Dynamic Nuclear Polarization at Temperatures up to 200 K. *Journal of the American Chemical Society* **2013,** *135* (34), 12790-12797.
39. Zhao, X. S.; Lu, G. Q.; Whittaker, A. K.; Millar, G. J.; Zhu, H. Y., Comprehensive Study of Surface Chemistry of MCM-41 Using ^{29}Si CP/MAS NMR, FTIR, Pyridine-TPD, and TGA. *The Journal of Physical Chemistry B* **1997,** *101* (33), 6525-6531.
40. Trébosc, J.; Wiench, J. W.; Huh, S.; Lin, V. S. Y.; Pruski, M., Solid-State NMR Study of MCM-41-type Mesoporous Silica Nanoparticles. *J. Am. Chem. Soc.* **2005,** *127* (9), 3057-3068.
41. Ghanbari-Siahkali, A.; Philippou, A.; Dwyer, J.; Anderson, M. W., The Acidity and Catalytic Activity of Heteropoly Acid on MCM-41 Investigated by MAS NMR, FTIR And Catalytic Tests. *Applied Catalysis A: General* **2000,** *192* (1), 57-69.

42. Sutra, P.; Fajula, F.; Brunel, D.; Lentz, P.; Daelen, G.; Nagy, J. B., ^{29}Si and ^{13}C MAS-NMR Characterization of Surface Modification of Micelle-Templated Silicas during the Grafting of Organic Moieties and End-Capping. *Colloids and Surfaces A: Physicochemical and Engineering Aspects* **1999,** *158* (1), 21-27.
43. Wouters, B. H.; Chen, T.; Dewilde, M.; Grobet, P. J., Reactivity of the Surface Hydroxyl Groups of MCM-41 towards Silylation with Trimethylchlorosilane. *Microporous Mesoporous Mater.* **2001,** *44-45*, 453-457.
44. Laha, S. C.; Kadgaonkar, M. D.; Anuji, A.; Ganapathy, S.; Amoureux, J. P.; Kumar, R., Multinuclear Solid-State MAS/CP-MAS NMR Studies of Promoter (Phosphate)-Enhanced Crystallization of Siliceous MCM-41. *The Journal of Physical Chemistry B* **2003,** *107* (51), 14171-14175.
45. Zhao, X. S.; Audsley, F.; Lu, G. Q., Irreversible Change of Pore Structure of MCM-41 upon Hydration at Room Temperature. *The Journal of Physical Chemistry B* **1998,** *102* (21), 4143-4146.
46. Beck, J. S.; Vartuli, J. C.; Roth, W. J.; Leonowicz, M. E.; Kresge, C. T.; Schmitt, K. D.; Chu, C. T. W.; Olson, D. H.; Sheppard, E. W.; McCullen, S. B.; Higgins, J. B.; Schlenker, J. L., A New Family of Mesoporous Molecular Sieves Prepared with Liquid Crystal Templates. *J. Am. Chem. Soc.* **1992,** *114* (27), 10834-10843.
47. Lippmaa, E.; Maegi, M.; Samoson, A.; Engelhardt, G.; Grimmer, A. R., Structural Studies of Silicates by Solid-State High-Resolution Silicon-29 NMR. *J. Am. Chem. Soc.* **1980,** *102* (15), 4889-4893.
48. Cookson, D. J.; Smith, B. E., Atmospheric Oxygen as the Dominant Source of ^{29}Si Spin-Lattice Relaxation in Solid Silicalite. *Journal of Magnetic Resonance (1969)* **1985,** *63* (1), 217-218.
49. Klinowski, J.; Carpenter, T. A.; Thomas, J. M., The Origin of ^{29}Si Spin–Lattice Relaxation in Zeolites: A Means of Rapid Acquisition of N.M.R. Spectra and of Probing Internal Sites in Microporous Catalysts. *J. Chem. Soc., Chem. Commun.* **1986,** (12), 956-958.
50. Pump, E.; Viger-Gravel, J.; Abou-Hamad, E.; Samantaray, M. K.; Hamzaoui, B.; Gurinov, A.; Anjum, D. H.; Gajan, D.; Lesage, A.; Bendjeriou-Sedjerari, A.; Emsley, L.; Basset, J.-M., Reactive Surface Organometallic Complexes Observed Using Dynamic Nuclear Polarization Surface Enhanced NMR Spectroscopy. *Chemical Science* **2017,** *8* (1), 284-290.
51. Rossini, A. J.; Zagdoun, A.; Hegner, F.; Schwarzwälder, M.; Gajan, D.; Copéret, C.; Lesage, A.; Emsley, L., Dynamic Nuclear Polarization NMR Spectroscopy of Microcrystalline Solids. *J. Am. Chem. Soc.* **2012,** *134* (40), 16899-16908.
52. Pines, A.; Gibby, M. G.; Waugh, J. S., Proton‐Enhanced NMR of Dilute Spins in Solids. *The Journal of Chemical Physics* **1973,** *59* (2), 569-590.
53. Maciel, G. E.; Sindorf, D. W., Silicon-29 NMR Study of the Surface of Silica Gel by Cross Polarization and Magic-Angle Spinning. *J. Am. Chem. Soc.* **1980,** *102* (25), 7606-7607.
54. Shenderovich, I. G.; Buntkowsky, G.; Schreiber, A.; Gedat, E.; Sharif, S.; Albrecht, J.; Golubev, N. S.; Findenegg, G. H.; Limbach, H.-H., Pyridine-^{15}N A Mobile NMR Sensor for Surface Acidity and Surface Defects of Mesoporous Silica. *The Journal of Physical Chemistry B* **2003,** *107* (43), 11924-11939.
55. Brouwer, D. H.; Kristiansen, P. E.; Fyfe, C. A.; Levitt, M. H., Symmetry-Based ^{29}Si Dipolar Recoupling Magic Angle Spinning NMR Spectroscopy: A New Method for Investigating Three-Dimensional Structures of Zeolite Frameworks. *Journal of the American Chemical Society* **2005,** *127* (2), 542-543.

56. Corma, A.; Diaz-Cabanas, M. J.; Martinez-Triguero, J.; Rey, F.; Rius, J., A Large-Cavity Zeolite with Wide Pore Windows and Potential as an Oil Refining Catalyst. *Nature* **2002,** *418* (6897), 514-517.
57. Maligal-Ganesh, R. V.; Xiao, C.; Goh, T. W.; Wang, L.-L.; Gustafson, J.; Pei, Y.; Qi, Z.; Johnson, D. D.; Zhang, S.; Tao, F.; Huang, W., A Ship-in-a-Bottle Strategy To Synthesize Encapsulated Intermetallic Nanoparticle Catalysts: Exemplified for Furfural Hydrogenation. *ACS Catalysis* **2016**, *6* (3),1754-1763.
58. Hayashi, S.; Hayamizu, K., Chemical Shift Standards in High-Resolution Solid-State NMR (1) ^{13}C, ^{29}Si, and ^{1}H nuclei. *Bull. Chem. Soc. Jpn.* **1991,** *64* (2), 685-687.
59. Kristiansen, P. E.; Carravetta, M.; Beek, J. D. v.; Lai, W. C.; Levitt, M. H., Theory and Applications of Supercycled Symmetry-Based Recoupling Sequences in Solid-State Nuclear Magnetic Resonance. *The Journal of Chemical Physics* **2006,** *124* (23), 234510.

TOC

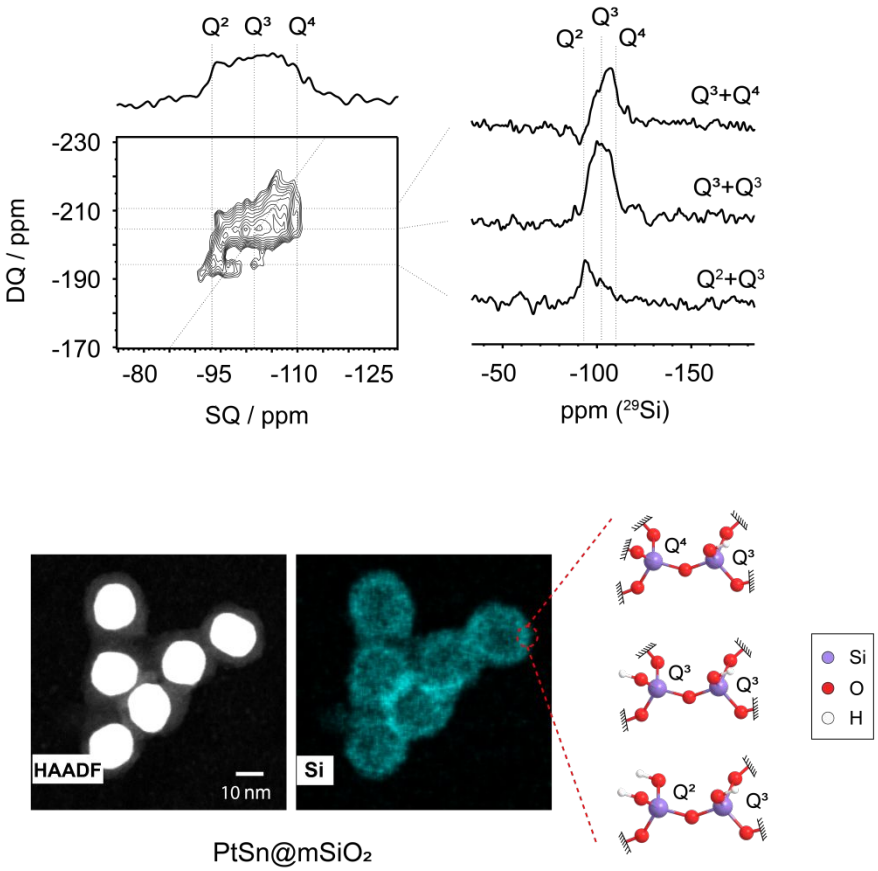
Q² Q³ Q⁴
-230
-210
-190
-170
DQ / ppm
-80 -95 -110 -125
SQ / ppm
Q³
Q² Q⁴
Q³+Q⁴
Q³+Q³
Q²+Q³
-50 -100 -150
ppm (²⁹Si)
HAADF
10 nm
Si
Q⁴ Q³
Q³ Q³
Q² Q³
Si
O
H
PtSn@mSiO₂